Morphometry of Dendritic Materials in Rechargeable Batteries Part I: Kinetics

Asghar Aryanfar *†‡, Sajed Medlej †, *Rudolph Marcus* §

† *American University of Beirut, Riad El-Solh, Lebanon 1107 2020*
‡ *Bahçeşehir University, 4 Çırağan Cad, Beşiktaş, Istanbul, Turkey 34353*
§ *California Institute of Technology, 1200 E California Blvd, Pasadena, CA 91125*

Abstract

The formation of highly-branched dendrites during the charging period of the rechargeable batteries is a critical safety drawback, causing capacity decay in particular during utilization of high energy-density metallic elements as electrode. We develop a comparative framework for predicting the branching tendency of the conventional metallic candidates in connection with their inherent material properties as well as spatial parameters. The development is established from the kinetic aspect of the electrodeposition, where the brownian motion leads to the random formation of highly porous microstructures. The ionic species are reduced in the proximity of the dendrite body and turn into the atom with the success probability derived from the electron transfer principles. Our development has been carried out in the atomic scale ($\sim \mathring{A}$) and the time interval of inter-ionic collisions ($\sim ps$) and the determining sub-factors leading to branched evolution are analyzed separately. The results provide intuitive understanding for the effective utilization of the electrode materials in rechargeable batteries based in the in the given specific application and environment.

Keywords: Dendritic evolution, electrodeposition, electrode materials, reaction probability.

1   Introduction

The modern era of wireless revolution and portable electronics demands the utilization of reliable intermittent renewables and long-lasting electrical energy storage facilities [4, 5]. As well, the growing demand for portable computational power as well as the introduction of electric vehicles demand novel and reliable high capacity energy storage devices. Despite such impressive growth of the need in the daily

---

*Corresponding author; email: aryanfar@caltech.edu

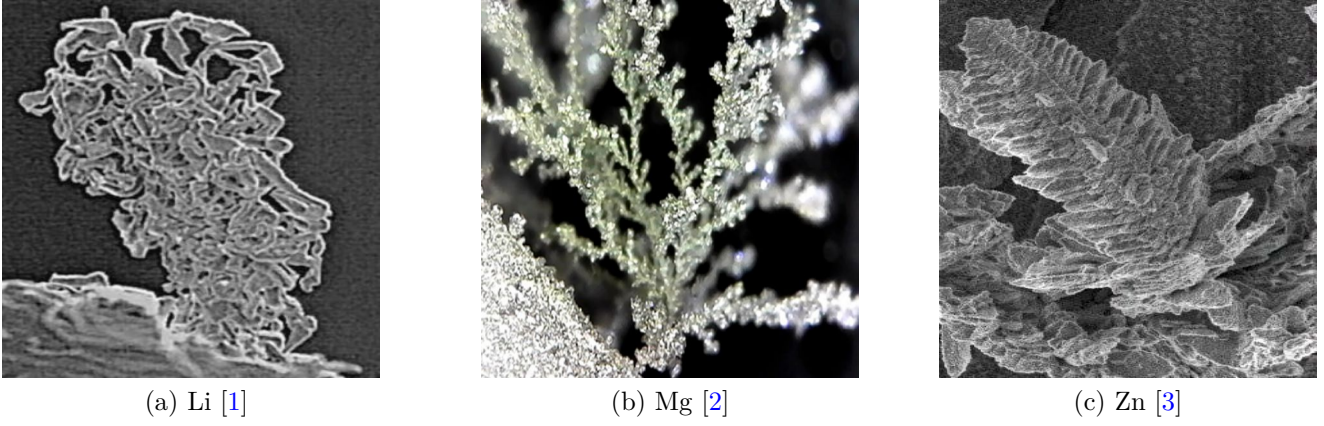|		
(a) Li [1]	(b) Mg [2]	(c) Zn [3]

Figure 1: Dendritic evolution for the demanded electrode materials.

lifestyle, the underlying science remains to be developed. Rechargeable batteries, which retrieve/store energy from/within the chemical bonds, have proven the be the most reliable and cleanest resource of electrical energy for the efficient management of the power. [6, 7] Metallic anodes such as lithium Li [8], sodium Na [9], magnesium Mg [2], and zinc Zn [10] are arguably highly attractive candidates for use in high-energy and high-power density rechargeable batteries. Lithium Li possess the lowest mass density ($\rho_{Li} = 0.53$ $g.cm^{-3}$) and the highest electropositivity ($E^0 = -3.04V$ vs SHE[1]) which provides the highest gravimetric energy density and likely the highest voltage output, making it suitable for high-power applications such as electric vehicles [11, 12, 13]. Sodium has a lower cost and is more earth abundant and is operational for large-scale stationary energy storage applications [14]. Magnesium Mg possess a high specific capacity and reactivity [15] whereas Zinc Zn is earth-abundant, has low cost and high storage capacity [16].

During the charging, the fast-pace formation of microstructures with relatively low surface energy from Brownian dynamics, leads to the branched evolution with high surface to volume ratio [12]. The quickening tree-like morphologies could occupy a large volume, possibly reach the counter-electrode and short the cell. Additionally, they can also dissolve from their thinner necks during subsequent discharge period and form detached dead crystals, leading to thermal instability and capacity decay [17, 18]. Such a formation-dissolution cycle is particularly prominent for the metal electrodes due to lack of intercalation [19], where the depositions in the surface is the only dominant formation mechanism versus the diffusion into the inner layers as the housing [20]. The growing amorphous crystals can pierce into the polymer electrolyte and short the cell afterwards, given their higher porosity, they could have mechanical properties comparable to the bulk form [21].

Previous studies have investigated various factors on dendritic formation such as current density [22], electrode surface roughness [23, 24], impurities [25], solvent and electrolyte chemical composition [26, 27], electrolyte concentration [28], utilization of powder electrodes [29] and adhesive polymers[30], temperature [31, 32], guiding scaffolds [33, 34], capillary pressure [35], cathode morphology [36] and mechanics [37, 38, 39, 40]. Some of conventional characterization techniques used include NMR [41] and

---

[1]SHE: Standard Hydrogen Electrode, taken conventionally as the reference ($E^0_{H^2} = 0$)
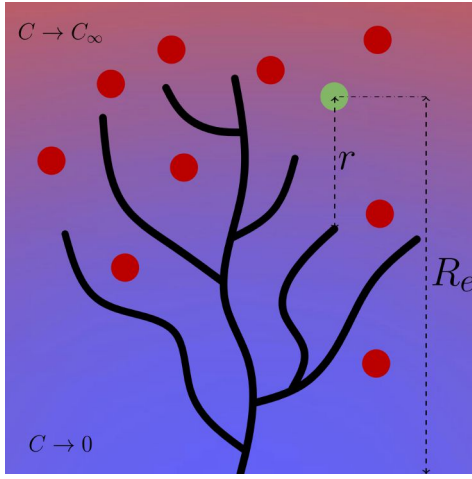
(a) Illustration of the spatial variants. $\{r, R_e, K_m\}$.
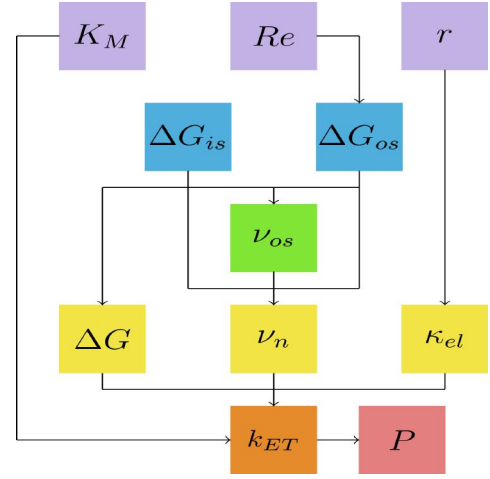
(b) Flowchart of connection to material and solvent properties.

Figure 2: Schematics of the parameters and their inter-connection.

MRI. [42] Recent studies also have shown the necessity of stability of solid electrolyte interphase (i.e. SEI) layer for controlling the nucleation and growth of the branched medium [43, 44] as well as pulse charging [45, 46, 47].

Earlier model of dendrites had focused on the electric field and space charge as the main responsible mechanism [48] while the later models focused on ionic concentration causing the diffusion limited aggregation (DLA). [49, 50, 51, 52] Both mechanisms are part of the electrochemical potential [53, 54], indicating that each could be dominant depending on the localizations of the electric potential or ionic concentration within the medium. Recent studies have explored both factors and their interplay, particularly in continuum scale and coarser time intervals, matching the scale of the experimental time and space [55]. Other simplified frameworks include phase field modeling [56, 57, 58] and analytical developments [59].

During charge period the ions accumulate at the dendrites tips (unfavorable) due to high electric field in convex geometry and at the same time tend to diffuse away to other less concentrated regions due to diffusion (favorable). Such dynamics typically occurs within the double layer (or stern layer [60]) which is relatively small and comparable to the Debye length. In high charge rates, the ionic concentration is depleted on the reaction sites and could tend to zero [52]; Nonetheless, our continuum-level study extends to larger scale, beyond the double layer region [61].

In this paper, we elaborate further on the tendency of the electrode materials for the formation and growth of dendritic (sub)branches. The candidate elements have already been utilized in primarily[2] batteries with potential applications in rechargeable alternatives. Our atomistic-scale ($\sim$ Å) approach quantifies the role of the location of ions as spatial variables (Figure 2a) and their connection to the

---

[2]i.e. non-rechargeable.

3

	Li	Na	Mg	Zn	Ref.	Solvent
$a_M(A^0)$ [3]	1.45	1.8	1.5	1.35	[62]	Ethylene
$a_{M^{n+}}(A^0)$	0.9	1.16	0.86	0.88	[63]	Carbonate
$\phi(eV)$	2.9	2.4	3.7	4.3	[64]	(EC)

Table 1: Atomistic properties of the electrode materials.

material properties on the kinetics of the ionic transport and electrodeposition (Figure 2a) which leads to the probability of the reaction and hence determines the ultimate form of the metastable dendrites.

2 Methodology

Table 1 shows the atomic scale properties of the electrode materials. The instigation of the dendrites is rooted in the non-uniformity of electrode surface morphology at the atomic scale combined with Brownian ionic dynamics during electrodeposition. Any asperity in the surface provides a sharp electric field that attracts the upcoming ions as a deposition sink. As well the closeness of a convex surface to the counter electrode, as the source of ionic release, would make such peaks more favorable sites, leading to further quickening growth of dendrites in any scale. Such a fast-pace formation leads to the evolution of highly branched medium with a high surface to volume ratio and porosity as high as $\approx 97\%$ [65].

The approaching ion M^{n+} to the dendrite body, is successfully deposited to metallic state M^0 with the probability of p according to the reaction 1:

$$M^{n+} + ne^- \rightarrow M^0 \tag{1}$$

where $M \in \{Li, Na, Mg, Zn\}$ and $n \in \{1, 2\}$. Respectively, such ion will move on and maintain original form with the probability of $1 - p$. Such probability p directly impacts the rate of electron transfer k_{ET} as [66]:

$$p = 1 - \exp\left(-k_{ET}\delta t\right) \tag{2}$$

where δt is the time interval given for the electron transfer. In fact the reaction probability of p controls the rate of the electron transfer k_{ET} in a given try:

$$0 \leq p < 1 \iff 0 \leq k_{ET} < \infty \tag{3}$$

Thus the higher values of p causes the initial approaches in the outer boundary of the dendrites more successful creating more branches and vice versa smaller probability p provides more likeliness for the upcoming ions to safely pass the boundary and diffuse into the inner layers, which makes the deposition more compact (i.e. less dendritic).

---

[3]Although the current study is for the amorphous dendritic crystals in mesoscale understanding, the atomic radius has been taken from the natural and ordered crystalline phase: $a \equiv 2r_{bond}$.

Var.	Li	Na	Mg	Zn	Ref.		Var.	Value	Ref.
$\varepsilon(meV)$	7.1	5.6	0.98	5.4	[68, 69]		ε_s	95.3	[70]
$\Delta a(\text{Å}^0)$	1.1	1.28	1.28	0.94	Eq. 6		ε_{opt}	1.84	[71]
$f(eV.\text{Å}^{-2})$	0.24	0.13	0.03	0.20	Eq. 8		$\nu_{is}(Hz)$	10^{13}	[72]
$\Delta G_{is}(meV)$	36.8	26.6	12.3	44.2	Eq. 7		$\tau_L(ps)$	0.21	Eq. 13

Table 2: General values.

The rate of electron transfer k_{ET} in the reaction 2 is expressed from Marcus theory as [53, 67]:

$$k_{ET} = K_M \nu_n \kappa_{el} \exp\left(\frac{-\Delta G}{k_B T}\right) \tag{4}$$

where K_m is the equilibrium constant, ν_n is the nuclear frequency factor, κ_{el} is the electron transmission coefficient and ΔG is the activation energy (i.e. energy barrier) for the reaction. We address these parameters extensively as below:

2.1 Activation Energy (ΔG)

From Equation 4 the electron transfer rate k_{ET} has the highest sensitivity to the energy barrier ΔG for the reduction of the ion into the sea of provided electrons within the already-deposited atoms. The energy barrier ΔG has two distinct compartments as [66]:

$$\Delta G = \Delta G_{out} + \Delta G_{in} \tag{5}$$

where ΔG_{is} and ΔG_{os} are the corresponding activation energy for the inner and outer shell electron transfer respectively.

The inner shell activation energy is obtained by assuming the bond as a spring that stretched from ionic to atomic bond length. Such change Δa during transition from ionic a_M and metallic $a_{M^{n+}}$ states would be:

$$\Delta a = a_M - a_{M^{n+}} \tag{6}$$

Therefore the stored inner-shell energy ΔG_{is} in general is the sum for all the bonds formed [72] as:

$$\Delta G_{is} = \frac{1}{2} \sum_{i=1}^{n} f_i \left(\frac{\Delta a}{2}\right)^2 \tag{7}$$

where f_i is the normal mode force constant, n is the number of formed bonds. The force constant f_i can be obtained from the Leonard Jones potential V_{LJ} relationship given as [73]:

$$V_{LJ} = \varepsilon \left[\left(\frac{a}{r}\right)^{12} - 2\left(\frac{a}{r}\right)^{6}\right]$$
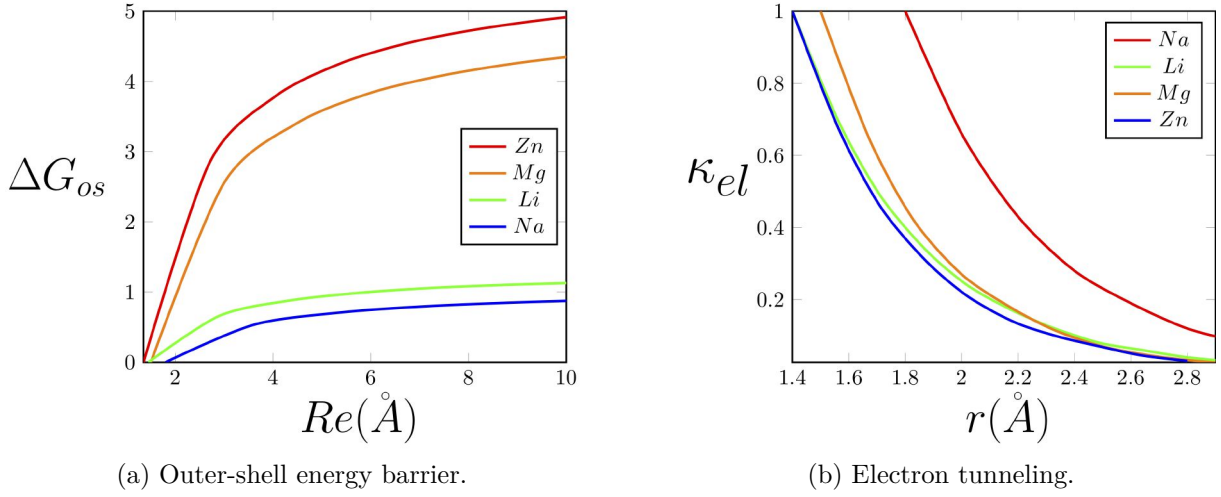
(a) Outer-shell energy barrier.

(b) Electron tunneling.

Figure 3: Distance-dependent variants.

where ε is the depth of potential well in the energy-distance diagram, a is the minimum-potential distance (a.k.a bond length), and r is the distance variable. The force constant f can be obtained from the second derivative of the potential distribution around the equilibrium distance ($r \approx a$) as: [4]

$$f = \left.\frac{\partial^2 V_{LJ}}{\partial r^2}\right|_{r=a} = \left.\frac{\partial}{\partial r}\left(\varepsilon\left(\frac{-12a^{12}}{r^{13}} + \frac{12a^6}{r^7}\right)\right)\right|_{r=a}$$

$$= \left.12\varepsilon\left(\frac{13a^{12}}{r^{14}} - \frac{7a^6}{r^8}\right)\right|_{r=a} = \frac{72\varepsilon}{a^2} \tag{8}$$

and the material-dependent parameters are calculated in the Table 2. The outer shell the activation energy ΔG_{os} is expressed as [72, 74]:

$$\Delta G_{os} = \frac{n^2 e^2}{8}\left(\frac{1}{a} - \frac{1}{R_e}\right)\left(\frac{1}{\varepsilon_{opt}} - \frac{1}{\varepsilon_s}\right) \tag{9}$$

where e is electron charge, n is valence electrons, a is the atomic radius, R_e is the distance of the reaction from the electrode surface and ε_{op} and ε_s are optical and static permittivity of the solvent. Figure 3a visualizes the relation of the outer-shell energy barrier ΔG_{os} to the distance from the electrode R_e.

---

[4]Equivalent to the energy stored in a spring, stretched infinitesimally to the distance of δ, where: $U = \frac{1}{2}k\delta^2$, hence the stiffness k is obtained as $\frac{\partial^2 U}{\partial \delta^2} = k$.

Var.	Li	Na	Mg	Zn	Ref.		Var.	Value	Ref.
K_m		0.5			Eq. 10		$R_e(\text{Å})$	5	Fig. 2a
$r(\text{Å})$	2.9	3.6	3.0	2.7	Fig. 2a ($\sim$ 2a)		$\delta t(ps)$	0.01	[77]
$\Delta G_{os}(meV)$	32.6	23.7	124	144	Eq. 9		$D(m^2/s)$	1.4×10^{-14}	[55]
$\Delta G(meV)$	69.4	50.3	137	188	Eq. 5		$\#Li^+$	50	[55]
$\nu_n(THz)$	7.4	7.3	4.1	5.6	Eq. 11		$\#Li^0$	400	[55]
$\kappa_{el}(\times 10^{-3})$	80.0	57.7	52.3	57.1	Eq. 14		$\Delta t(\mu s)$	1	[55]
$k_{ET}(GHz)$	19.7	29.8	0.527	0.105	Eq. 4		$l(nm)$	167	[55]
p	0.861	0.949	0.051	0.010	Eq. 2		$\Delta V(mV)$	85	[55]

Table 3: Sample computation parameters.

2.2 Concentration ratio (K_m)

The equilibrium constant K_M represents the ratio of *local-to-bulk* concentration in the precursor state ($K_M := \dfrac{C_{local}}{C_\infty}$). Therefore the range of this ratio is:

$$0 \leq K_M \leq 1 \tag{10}$$

During steady-state depletion in the reaction site, such concentration distribution is computed for flat electrodes (i.e. linear distribution) [48, 49] as well as curved surfaces [61], reducing from the ambient electrolyte concentration C_∞ to 0 in redox sites.

2.3 Nuclear frequency factor (ν_n)

The nuclear frequency factor ν_n represents the rates of attempts on the energy barrier ΔG and correlates with the bond vibration and solvent motion. Assuming stagnant solvent in the steady state condition, we can obtain the nuclear frequency factor ν_n via quadratic interpolation of activation energies in the inner ΔG_{is} and outer ΔG_{os} shells as [75]:

$$\nu_n = \sqrt{\frac{\nu_{is}^2 \Delta G_{is} + \nu_{os}^2 \Delta G_{os}}{\Delta G_{is} + \Delta G_{os}}} \tag{11}$$

where ν_{is} is the frequency value of attempts in the inner shell, given in Table 1. The frequency of tries on the outer shell ν_{os} correlates additionally with the solvent as:

$$\nu_{os} = \tau_L^{-1} \sqrt{\frac{\Delta G_{os}}{4\pi k_B T}} \tag{12}$$

where τ_L is the period for the solvent relaxation, scaled from Debye relaxation time τ_D as [76]:

$$\tau_L = \frac{\varepsilon_\infty}{\varepsilon_s} \tau_D \tag{13}$$

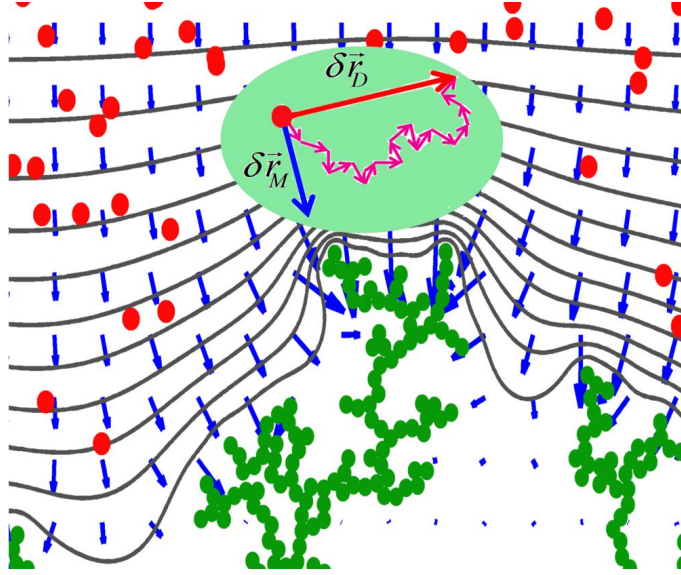where ε_∞ is the high frequency dielectric constant.

Figure 4: The transport elements in the coarse scale of time and space. green: dendrite atoms, red: free ions, blue: electric field, black: iso-potential contours.

2.4 Electron transmission (κ_{el})

The electronic transmission coefficient represents the probability of electron tunneling as [72]:

$$\kappa_{el} = \kappa_{el}^0 \exp\left(-\frac{4\pi\sqrt{2m_e\phi}}{\hbar}(r-a)\right) \tag{14}$$

where κ_{el}^0 is the pre-factor, assumed to be unity for adiabatic processes, m_e and $\hbar$ are the electron mass and plank constant, r is donor-acceptor separation distance, a is separation distance of closest approach (i.e. interatomic distance), and ϕ is the work function. The tunneling probability is visualized versus distance in the Figure 3b.

2.5 Sample Computation

We have utilized the Coarse-grained method in time and space for the simulation of the dendrite morphology [55]. In this context, the electrochemical flux is typically generated either due the gradients of concentration (∇C) or electric potential (∇V). The convection is negligible in atomic scale, since Rayleigh number Ra which is highly dependent to the scale (i.e. $Ra \propto l^3$) is very small for the thin layer of electrodeposition: $Ra < 1500$ [78]. In the ionic scale, the regions of higher concentration tend to collide and repel more and, given enough time, disperse to lower concentration zones. In the larger scale, such inter-collisions could be added-up and be represented by the diffusion length [61]. Such displacements during the coarse time interval Δt could reach to $\sim ms$ where the ionic inter-collision time is typically in the order of $\sim fs$ ($\Delta t = \sum_{i=1}^{n} \delta t_i$). Therefore, the movement of each ionic specie $\delta\vec{\mathbf{r}}$ would be:

$$\delta\vec{\mathbf{r}} = \sqrt{2D^+\Delta t}\ \hat{\mathbf{g}} + \mu^+\vec{\mathbf{E}}\Delta t \tag{15}$$
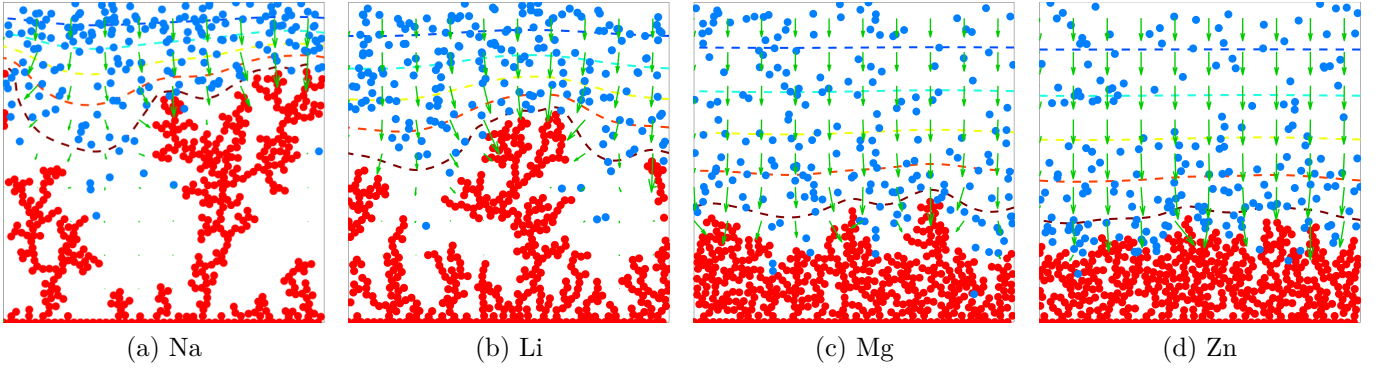
8

Figure 5: Obtained morphologies of the electrode materials.

where D^+ is the ionic diffusion coefficient in the electrolyte, $\hat{\mathbf{g}}$ is a normalized vector in random direction, representing the Brownian dynamics and μ^+ is the mobility of cations in electrolyte, obtained from Einstein relation ($\mu = \dfrac{D}{k_B T}$), and the local electric field $\vec{\mathbf{E}}$ is the gradient of electric potential ($\vec{\mathbf{E}} = -\nabla V$). The diffusion length represents the average progress of a diffusive wave in a given time Δt, obtained directly from the continuum-scale description of diffusion [79]. The large-scale movements in the Equation 15 is schematically illustrated in the Figure 4, where the infinitesimal displacements are summed into the coarse grained vector.

Using the material-dependent parameters, given and obtained in Tables 1 and 2 and assuming typical and trivial values for spatial parameters of concentration ratio K_m, the donor-acceptor distance r and the distance from the electrode R_e one can reach to the rate of the electron transfer k_{ET} and the corresponding probability of the reaction p, which have been provided in the Table 3. Combining the evolution dynamics (Eq. 15) with the description probability of the electron transfer (Eq. 2) the stochastically grown morphology of the dendritic trees are computed and illustrated in the Figure 5. As well, we define a density measure ρ, which shows the fraction of filled space in the dendrite zone as:

$$\rho = \frac{N \pi a^2}{4 h_{max} l}$$

where N is number of atoms in the dendrite body, h_{max} is the maximum reach of the dendrite atoms from the electrode and l is the domain scale. The higher values of the density ρ represent the more favorable and less branched microstructure.

3   Results & Discussion

The probability of successful jump p, which in a larger scale controls the rate of electron transfer k_{ET} is a critical factor in determining the ultimate morphology of the growing dendrites. The higher probability p causes more successful initial success rates upon reaching the dendrite and the branched morphology is developed from the outer regions (i.e. fingers), whereas the lower probability of jump p provides more

chance for the upcoming ionic species to infiltrate the inner layers of the microstructure and fill the voids, leading to more packed morphology. Therefore:

$$p \uparrow \ \sim \ \rho \downarrow \ \text{(dendritic)}$$

We have described such probability of success p in terms of the inherent *material* properties as well as *spatial* variants as below:

3.1 Material Properties

The underlying attribute of the material, given separately in the Table 1 are described as below:

Work function (ϕ)

The work function ϕ is the minimum thermodynamics work needed to remove an electron from the material to the outer vacuum space [80], and the following order holds between the electrode materials [64]:

$$\phi: \ Zn > Mg > Li > Na \tag{16}$$

Such property reveals the tendency of the atom to keep the electron before giving away. Thus, the higher value of the work function ϕ leads to lower probability of electron tunneling κ_{el} (Eq. 14, Fig. 3b), causing the lower probability of electron transfer p. Such trend would make less dendritic microstructure, therefore:

$$\phi \uparrow \ \sim \ \kappa_{el} \downarrow \ \sim \ p \downarrow \ \text{(packed)} \tag{17}$$

Valence Electrons (n)

The energy barrier needed for the reduction reaction 1 directly correlates with the valence electrons n based on the outer-shell activation energy (Eq. 9), which gives the advantage for the higher valence electron materials as ordered below:

$$n: \ Zn = Mg > Li = Na \tag{18}$$

Higher valence electrons n quadratically increase the outer shell activation energy ΔG_{os} (Eq. 9) which is illustrated in the Figure 3a. Therefore possibility of successful bonding p is reduced, leading to more packed morphology:

$$n \uparrow \ \sim \ \Delta G \uparrow \ \sim \ p \downarrow \ \text{(packed)} \tag{19}$$

(a) Donor-acceptor distance r: $R_e = a(\text{solid}), 2a(\text{dashed}), K_m = 0.5$.

(b) Distance from electrode R_e: $K_m = 0.5(\text{dashed}), 0.75(\text{solid}), r = 2a$.
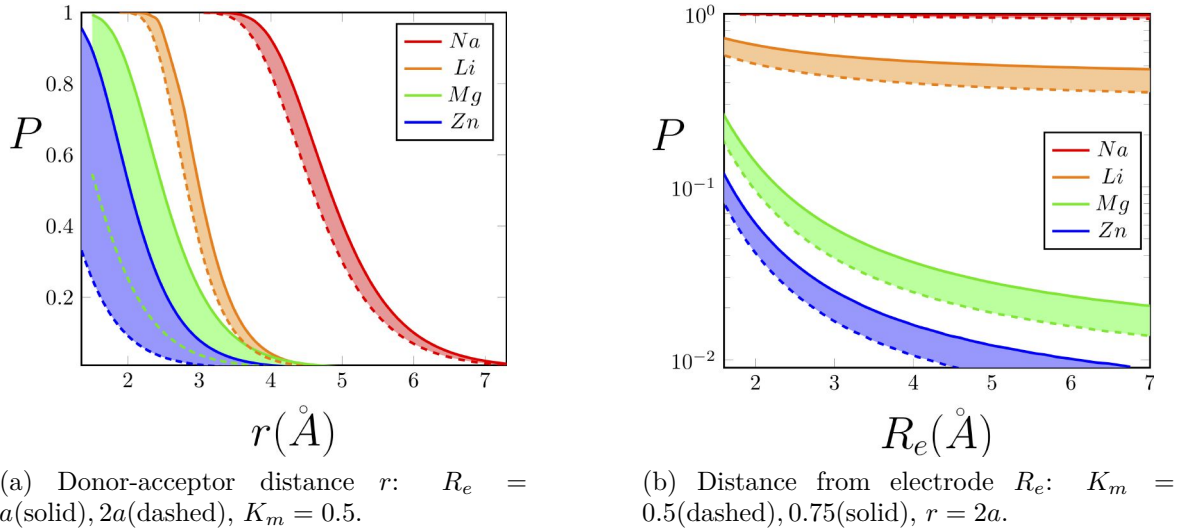
Figure 6: The behavior of reaction probability versus the spatial variables.

Atomic radius (a)

The size of atom - and the corresponding ion - are effective parameters for the reaction since the large atomic size can instigate higher possibility of overlap and electron transfer. The outer-shell energy barrier ΔG_{os} (Eq. 9) in fact measures the potential energy difference between when the ionic M^{n+} and metallic M species reach in the atomic distance a versus a reference potential, determined by the distance from the electrode R_e. Therefore the bond distance a directly impact the energy barrier and the materials are ordered as follows:

$$a: \ Na > Mg > Li > Zn \tag{20}$$

Notably, increasing the overlap possibility due to larger atomic size a leads to a branched evolution, whereas the smaller atoms could possibly escape more from the branches and infiltrate the inner sites. On the other hand the atomic size a directly correlates with the probability of the electron tunneling κ_{el} (Eq. 14). Hence:

$$a \uparrow \ \sim \ \kappa_{el} \uparrow, \Delta G \downarrow \ \sim \ p \uparrow \ (\text{Dendritic}) \tag{21}$$

The other size-dependent parameter is the inner-shell activation energy ΔG_{is} (Eq. 7) which is considered as a spring of stiffness f stretched between the ionic and atomic values Δa (Eq. 6) and due to symmetry the half value is in effect (i.e. $\dfrac{\Delta a}{2}$).

Figure 5 shows that sodium Na has the highest tendency for the formation of dendritic microstructures. The lower energy barrier of the sodium Na has previously provided identical insight [81], particularly in the context of surface-diffusion relative to lithium Li and magnesium Mg [82, 83].
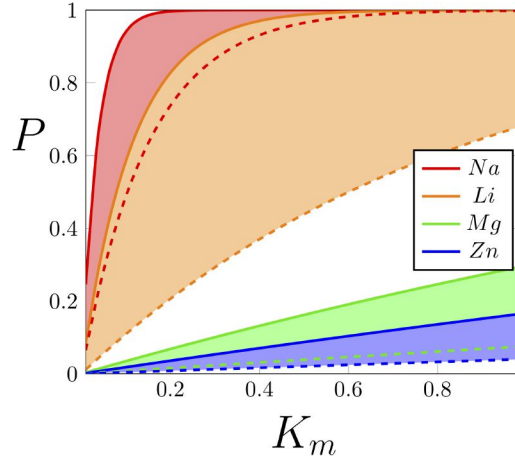
11

Figure 7: Probability vs concentration ratio K_m: $r = 1.5a(\text{dashed}), 2a(\text{solid})$, $R_e = 2a$

3.2 Spatial variants

The spatial variants in the Figure 2a and the flowchart 2b are location-dependent parameters shown as below:

Donor-acceptor distance (r)

While atoms and ions collide and repel due to Brownian dynamics, the real-time distance r between the donor and acceptor is a critical parameter which exponentially correlates with the success rate of the electron tunneling κ_{el} (Eq. 14). The electron from the donor is contained in the atom within the dendrite body shared as part of sea of electrons where the electron acceptor is the ionic specie approaching the dendrite body. Thus:

$$r \uparrow \ \sim \ \kappa_{el} \downarrow \ \sim \ p \downarrow \ (\text{packed}) \tag{22}$$

The exponential behavior of the electron tunneling κ_{el} versus the donor-acceptor distance r (Fig. 3b) finally translates into the probability of successful reaction p shown in the Figure 6a. Experiment-wise an important factor controlling the dynamics of the donor-acceptor distance r can be the current density of the electrodeposition j (as well as the voltage V), where the higher current rate leads to closer distances r and consequently forms the dendritic trees [84, 85, 23]. Particularly, during the initiation of dendrites, the ordered lattice crystal structure on the base of deposition could be a source for determining such distance where higher lattice density can provide closer proximity to the upcoming ions. In this manner, the magnesium Mg provides larger distances than lithium Li and leading to a lower migration energy barrier for electron jump [86].

Location of the reaction (R_e)

The distance of the reaction from the electrode surface R_e, in fact determines the reference potential for the outer shell energy barrier ΔG_{os} and therefore the total activation energy ΔG (Eq. 5). In this

12

Variant	r	R_e	K_m
Lab-scale Equivalent	Applied current I , Voltage V	Utilized charge Q	Concentration C

Table 4: Experimental equivalent for the analyzed variants.

manner, the further locations from the electrode surface would require higher activation energy ΔG_{os} (Eq. 9) and therefore the probability of electron transfer decreases, leading to more favorable uniform evolution of morphology:

$$R_e \uparrow \ \sim \ \Delta G_{os} \uparrow \ \sim \ p \downarrow \ \text{(packed)} \tag{23}$$

Therefore this factor is favorable for outer regions as illustrated in the Figure 6b and the sensitivity location of the reaction R_e is the highest in regions closer to the electrode (i.e. thin layer deposition).

Concentration Ratio K_m

As the reaction 1 occurs, the regions closer to the electrode surface deplete the ions and therefore the concentration is reduced, merely in the double layer region, where it could reach to zero in the limit of current density [48, 49, 61]. Therefore, starting from the electrode, the ionic concentration will have increasing trend toward ambient electrolyte. Typically the higher concentration leads to the higher rate of interactions and therefore the possibility of electron jump increases, leading to more dendritic morphology [87, 88, 89, 90]:

$$K_m \uparrow \ \sim \ p \uparrow \ \text{(dendritic)} \tag{24}$$

The illustration of the increasing trend is shown in the Figure 7 for the materials considered. Likewise the concentration of the charge carriers correlates directly with the concentration the counter-ions as they both compose the solvent shell [91]. Although the branching factor is similar in all cases (~ 2)[5] the branching propensity is higher in the locations further from the surface of the electrode.

Ultimately, the final morphology would depend on the combinatorics effects of the inherent *material* as well as *spatial* properties and each individual factor becomes effective in a given circumstance based on the application. We provide the experimental equivalence to the spatial variants analyzed in Table 4:

4 Conclusions

In this paper, we quantified the amorphous evolution of the dendritic microstructures for the popular electrode materials during the charging of the battery. The density of the electro-deposits which is a measure for the state-of-health, correlates inversely with the probability of successful electron transfer, which is a multi-variable quantity per see. The individual role of the material properties as well as

---

[5]Branching factor is the number of successors generated by a given branch.

the spatial (i.e. geometric) variants have been analyzed and correlated with the branching tendency. Our framework can be utilized for the selection process of the electrode materials in the given specific application where the prominent factor is either the utilized charge, the applied current density, or the thickness of the electro-deposited films.

List of Symbols

a_M, $a_{M^{n+}}$: Atomic and ionic radii (Å)

ϕ: Work function (V)

p: Probability of electron transfer([])

k_{ET}: Rate of electron transfer (s^{-1})

K_m: Local-to-bulk concentration ratio ([])

ν_n: Nuclear frequency factor (s^{-1})

ν_{is}: Inner-shell frequency (s^{-1})

ν_{os}: Outer-shell frequency (s^{-1})

κ_{el}: Probability of electron tunneling ([])

ΔG: Total activation energy (eV)

ΔG_{is}: Inner-shell energy barrier (eV)

ΔG_{os}: Outer-shell energy barrier (eV)

k_B: Boltzmann constant (1.38×10^{-23} $m^2.kg.s^{-2}.K^{-1}$)

T: Temperature ($298K$)

D: Diffusion coefficient (m^2/s)

C_∞: ambient electrolyte concentration (M)

e: electron charge ($1eV$)

τ_L: Period of solvent relaxation (s)

τ_D: Debye relaxation time (s)

ε_{op}: Optical permittivity of solvent ([])

ε_s: Static permittivity of solvent ([])

j: Current density ($mA.cm^{-2}$)

n: Valence electrons ([])

r: Donor-acceptor distance (Å)

R_e: Distance of the reaction from the electrode (Å)

m_e: Electron mass ($9.1 \times 10^{-31}kg$)

N: Number of deposited atoms

δt: Inter-ionic collision time (s)

Δt: Coarse-scale inter-ionic collision time (s)

h_{max}: Maximum reach of the dendrite from the electrode (Å)

ρ: The density of the dendrite ([])

l: Domain length (Å)

$\hbar$: Planck's constant ($4.1 \times 10^{-15}eV.s^{-1}$)

ε_0: Vacuum permittivity ($e^2eV^{-1}Å^{-1}$)

References

[1] F. Orsini A.D. Pasquier B. Beaudoin J.M. Tarascon et al. In situ scanning electron microscopy (sem) observation of interfaces with plastic lithium batteries. *J. Power Sources*, 76:19–29, 1998.

[2] Rachel Davidson, Ankit Verma, David Santos, Feng Hao, Coleman Fincher, Sisi Xiang, Jonathan Van Buskirk, Kelvin Xie, Matt Pharr, Partha P Mukherjee, et al. Formation of magnesium dendrites during electrodeposition. *ACS Energy Letters*, 4(2):375–376, 2018.

[3] Keliang Wang, Pucheng Pei, Ze Ma, Huicui Chen, Huachi Xu, Dongfang Chen, and Xizhong Wang. Dendrite growth in the recharging process of zinc–air batteries. *Journal of Materials Chemistry A*, 3(45):22648–22655, 2015.

[4] J. Rugolo and M. J. Aziz. Electricity storage for intermittent renewable sources. *Energy Environ. Sci.*, 5(5):7151–7160, 2012.

[5] Bruce Dunn, Haresh Kamath, and Jean-Marie Tarascon. Electrical energy storage for the grid: a battery of choices. *Science*, 334(6058):928–935, 2011.

[6] Rotem Marom, S Francis Amalraj, Nicole Leifer, David Jacob, and Doron Aurbach. A review of advanced and practical lithium battery materials. *Journal of Materials Chemistry*, 21(27):9938–9954, 2011.

[7] John B Goodenough and Kyu-Sung Park. The li-ion rechargeable battery: a perspective. *Journal of the American Chemical Society*, 135(4):1167–1176, 2013.

[8] Xin-Bing Cheng, Rui Zhang, Chen-Zi Zhao, and Qiang Zhang. Toward safe lithium metal anode in rechargeable batteries: a review. *Chemical reviews*, 117(15):10403–10473, 2017.

[9] Michael D Slater, Donghan Kim, Eungje Lee, and Christopher S Johnson. Sodium-ion batteries. *Adv. Funct. Mater.*, 23(8):947–958, 2013.

[10] Pucheng Pei, Keliang Wang, and Ze Ma. Technologies for extending zinc air batterys cyclelife: A review. *Applied Energy*, 128:315–324, 2014.

[11] Siyuan Li, Jixiang Yang, and Yingying Lu. Lithium metal anode. *Encyclopedia of Inorganic and Bioinorganic Chemistry*, pages 1–21.

[12] W. Xu, J. L. Wang, F. Ding, X. L. Chen, E. Nasybutin, Y. H. Zhang, and J. G. Zhang. Lithium metal anodes for rechargeable batteries. *Energy and Environmental Science*, 7(2):513–537, 2014.

[13] Aruna Zhamu, Guorong Chen, Chenguang Liu, David Neff, Qing Fang, Zhenning Yu, Wei Xiong, Yanbo Wang, Xiqing Wang, and Bor Z Jang. Reviving rechargeable lithium metal batteries: enabling next-generation high-energy and high-power cells. *Energy Environ. Sci.*, 5(2):5701–5707, 2012.

[14] Brian L Ellis and Linda F Nazar. Sodium and sodium-ion energy storage batteries. *Current Opinion in Solid State and Materials Science*, 16(4):168–177, 2012.

[15] Ivgeni Shterenberg, Michael Salama, Yossi Gofer, Elena Levi, and Doron Aurbach. The challenge of developing rechargeable magnesium batteries. *Mrs Bulletin*, 39(5):453–460, 2014.

[16] Yanguang Li and Hongjie Dai. Recent advances in zinc–air batteries. *Chem. Soc. Rev.*, 43(15):5257–5275, 2014.

[17] Kang Xu. Nonaqueous liquid electrolytes for lithium-based rechargeable batteries. *Chemical Reviews-Columbus*, 104(10):4303–4418, 2004.

[18] Deepti Tewari, Sobana P Rangarajan, Perla B Balbuena, Yevgen Barsukov, and Partha P Mukherjee. Mesoscale anatomy of dead lithium formation. *The Journal of Physical Chemistry C*, 2020.

[19] Zhe Li, Jun Huang, Bor Yann Liaw, Viktor Metzler, and Jianbo Zhang. A review of lithium deposition in lithium-ion and lithium metal secondary batteries. *J. Power Sources*, 254:168–182, 2014.

[20] MS Dresselhaus and G Dresselhaus. Intercalation compounds of graphite. *Advances in Physics*, 30(2):139–326, 1981.

[21] Asghar Aryanfar, Tao Cheng, and William A Goddard. Bulk properties of amorphous lithium dendrites. *ECS Transactions*, 80(10):365–370, 2017.

[22] Yaoyu Ren, Yang Shen, Yuanhua Lin, and Ce-Wen Nan. Direct observation of lithium dendrites inside garnet-type lithium-ion solid electrolyte. *Electrochemistry Communications*, 57:27–30, 2015.

[23] Christoffer P Nielsen and Henrik Bruus. Morphological instability during steady electrodeposition at overlimiting currents. *arXiv preprint arXiv:1505.07571*, 2015.

[24] PP Natsiavas, K Weinberg, D Rosato, and M Ortiz. Effect of prestress on the stability of electrode–electrolyte interfaces during charging in lithium batteries. *Journal of the Mechanics and Physics of Solids*, 95:92–111, 2016.

[25] J. Steiger, D. Kramer, and R. Monig. Mechanisms of dendritic growth investigated by in situ light microscopy during electrodeposition and dissolution of lithium. *J. Power Sources*, 261:112–119, 2014.

[26] N. Schweikert, A. Hofmann, M. Schulz, M. Scheuermann, S. T. Boles, T. Hanemann, H. Hahn, and S. Indris. Suppressed lithium dendrite growth in lithium batteries using ionic liquid electrolytes: Investigation by electrochemical impedance spectroscopy, scanning electron microscopy, and in situ li-7 nuclear magnetic resonance spectroscopy. *J. Power Sources*, 228:237–243, 2013.

[27] Reza Younesi, Gabriel M Veith, Patrik Johansson, Kristina Edström, and Tejs Vegge. Lithium salts for advanced lithium batteries: Li-metal, li-o 2, and li-s. *Energy and Environmental Science*, 8(7):1905–1922, 2015.

[28] Soon-Ki Jeong, Hee-Young Seo, Dong-Hak Kim, Hyun-Kak Han, Jin-Gul Kim, Yoon Bae Lee, Yasutoshi Iriyama, Takeshi Abe, and Zempachi Ogumi. Suppression of dendritic lithium formation by using concentrated electrolyte solutions. *Electrochemistry communications*, 10(4):635–638, 2008.

[29] I. W. Seong, C. H. Hong, B. K. Kim, and W. Y. Yoon. The effects of current density and amount of discharge on dendrite formation in the lithium powder anode electrode. *J. Power Sources*, 178(2):769–773, 2008.

[30] GM Stone, SA Mullin, AA Teran, DT Hallinan, AM Minor, A Hexemer, and NP Balsara. Resolution of the modulus versus adhesion dilemma in solid polymer electrolytes for rechargeable lithium metal batteries. *J. Electrochem. Soc.*, 159(3):A222–A227, 2012.

[31] Asghar Aryanfar, Tao Cheng, Agustin J Colussi, Boris V Merinov, William A Goddard III, and Michael R Hoffmann. Annealing kinetics of electrodeposited lithium dendrites. *The Journal of chemical physics*, 143(13):134701, 2015.

[32] Asghar Aryanfar, Daniel J Brooks, AgustÃn J Colussi, Boris V Merinov, William A Goddard III, and Michael R Hoffmann. Thermal relaxation of lithium dendrites. *Phys. Chem. Chem. Phys.*, 17(12):8000–8005, 2015.

[33] Yuanzhou Yao, Xiaohui Zhao, Amir A Razzaq, Yuting Gu, Xietao Yuan, Rahim Shah, Yuebin Lian, Jinxuan Lei, Qiaoqiao Mu, Yong Ma, et al. Mosaic rgo layer on lithium metal anodes for effective mediation of lithium plating and stripping. *Journal of Materials Chemistry A*, 2019.

[34] Ji Qian, Yu Li, Menglu Zhang, Rui Luo, Fujie Wang, Yusheng Ye, Yi Xing, Wanlong Li, Wenjie Qu, Lili Wang, et al. Protecting lithium/sodium metal anode with metal-organic framework based compact and robust shield. *Nano Energy*, 2019.

[35] Wei Deng, Wenhua Zhu, Xufeng Zhou, Fei Zhao, and Zhaoping Liu. Regulating capillary pressure to achieve ultralow areal mass loading metallic lithium anodes. *Energy Storage Materials*, 2019.

[36] Alexander W Abboud, Eric J Dufek, and Boryann Liaw. Implications of local current density variations on lithium plating affected by cathode particle size. *Journal of The Electrochemical Society*, 166(4):A667–A669, 2019.

[37] Markus Klinsmann, Felix E Hildebrand, Markus Ganser, and Robert M McMeeking. Dendritic cracking in solid electrolytes driven by lithium insertion. *Journal of Power Sources*, 442:227226, 2019.

[38] Chen Xu, Zeeshan Ahmad, Asghar Aryanfar, Venkatasubramanian Viswanathan, and Julia R Greer. Enhanced strength and temperature dependence of mechanical properties of li at small scales and its implications for li metal anodes. *Proceedings of the National Academy of Sciences*, 114(1):57–61, 2017.

[39] Peng Wang, Wenjie Qu, Wei-Li Song, Haosen Chen, Renjie Chen, and Daining Fang. Electro–chemo–mechanical issues at the interfaces in solid-state lithium metal batteries. *Advanced Functional Materials*, page 1900950, 2019.

[40] Guangyu Liu, Dandan Wang, Jianyu Zhang, Andrew Kim, and Wei Lu. Preventing dendrite growth by a soft piezoelectric material. *ACS Materials Letters*, 1(5):498–505, 2019.

[41] Rangeet Bhattacharyya, Baris Key, Hailong Chen, Adam S Best, Anthony F Hollenkamp, and Clare P Grey. In situ nmr observation of the formation of metallic lithium microstructures in lithium batteries. *Nat. Mater.*, 9(6):504, 2010.

[42] S Chandrashekar, Nicole M Trease, Hee Jung Chang, Lin-Shu Du, Clare P Grey, and Alexej Jerschow. 7li mri of li batteries reveals location of microstructural lithium. *Nat. Mater.*, 11(4):311–315, 2012.

[43] Yunsong Li and Yue Qi. Energy landscape of the charge transfer reaction at the complex li/sei/electrolyte interface. *Energy & Environmental Science*, 2019.

[44] Laleh Majari Kasmaee, Asghar Aryanfar, Zarui Chikneyan, Michael R Hoffmann, and AgustÃn J Colussi. Lithium batteries: Improving solid-electrolyte interphases via underpotential solvent electropolymerization. *Chem. Phys. Lett.*, 661:65–69, 2016.

[45] Jun Li, Edward Murphy, Jack Winnick, and Paul A Kohl. The effects of pulse charging on cycling characteristics of commercial lithium-ion batteries. *J. Power Sources*, 102(1):302–309, 2001.

[46] S Chandrashekar, Onyekachi Oparaji, Guang Yang, and Daniel Hallinan. Communication 7li mri unveils concentration dependent diffusion in polymer electrolyte batteries. *Journal of The Electrochemical Society*, 163(14):A2988–A2990, 2016.

[47] Asghar Aryanfar, Daniel J Brooks, and William A Goddard. Theoretical pulse charge for the optimal inhibition of growing dendrites. *MRS Advances*, 3(22):1201–1207, 2018.

[48] J. N. Chazalviel. Electrochemical aspects of the generation of ramified metallic electrodeposits. *Phys. Rev. A*, 42(12):7355–7367, 1990.

[49] C. Monroe and J. Newman. Dendrite growth in lithium/polymer systems - a propagation model for liquid electrolytes under galvanostatic conditions. *J. Electrochem. Soc.*, 150(10):A1377–A1384, 2003.

[50] Thomas A Witten and Leonard M Sander. Diffusion-limited aggregation. *Phys. Rev. B*, 27(9):5686, 1983.

[51] Xin Zhang, Q Jane Wang, Katharine L Harrison, Katherine Jungjohann, Brad L Boyce, Scott A Roberts, Peter M Attia, and Stephen J Harris. Rethinking how external pressure can suppress dendrites in lithium metal batteries. *Journal of The Electrochemical Society*, 166(15):A3639–A3652, 2019.

[52] V. Fleury. Branched fractal patterns in non-equilibrium electrochemical deposition from oscillatory nucleation and growth. *Nature*, 390(6656):145–148, 1997.

[53] Allen J. Bard and Larry R. Faulkner. Electrochemical methods: fundamentals and applications. 2 New York: Wiley, 1980., 1980.

[54] Deepti Tewari and Partha P Mukherjee. Mechanistic understanding of electrochemical plating and stripping of metal electrodes. *Journal of Materials Chemistry A*, 7(9):4668–4688, 2019.

[55] Asghar Aryanfar, Daniel Brooks, Boris V. Merinov, William A. Goddard Iii, AgustÃn J. Colussi, and Michael R. Hoffmann. Dynamics of lithium dendrite growth and inhibition: Pulse charging experiments and monte carlo calculations. *The Journal of Physical Chemistry Letters*, 5(10):1721–1726, 2014.

[56] Wenyu Mu, Xunliang Liu, Zhi Wen, and Lin Liu. Numerical simulation of the factors affecting the growth of lithium dendrites. *Journal of Energy Storage*, 26:100921, 2019.

[57] David R Ely, Aniruddha Jana, and R Edwin GarcÃa. Phase field kinetics of lithium electrodeposits. *J. Power Sources*, 272:581–594, 2014.

[58] Daniel A Cogswell. Quantitative phase-field modeling of dendritic electrodeposition. *Physical Review E*, 92(1):011301, 2015.

[59] Rohan Akolkar. Mathematical model of the dendritic growth during lithium electrodeposition. *J. Power Sources*, 232:23–28, 2013.

[60] Martin Z Bazant, Brian D Storey, and Alexei A Kornyshev. Double layer in ionic liquids: Overscreening versus crowding. *Phys. Rev. Lett.*, 106(4):046102, 2011.

[61] Asghar Aryanfar, Michael R Hoffmann, and William A Goddard III. Finite-pulse waves for efficient suppression of evolving mesoscale dendrites in rechargeable batteries. *Physical Review E*, 100(4):042801, 2019.

[62] John C Slater. Atomic radii in crystals. *The Journal of Chemical Physics*, 41(10):3199–3204, 1964.

[63] Robert D Shannon. Revised effective ionic radii and systematic studies of interatomic distances in halides and chalcogenides. *Acta crystallographica section A: crystal physics, diffraction, theoretical and general crystallography*, 32(5):751–767, 1976.

[64] FJ Lovas and LE Snyder. Crc handbook of chemistry and physics. *Internet Version 2008),(CRC, Boca Raton, FL), Sect*, 14(6), 2008.

[65] Asghar Aryanfar, Daniel J Brooks, Tao Cheng, Boris V Merinov, William A Goddard, Agustin J Colussi, and Michael R Hoffmann. Three dimensional modeling of dendrite growth in rechargeable lithium metal batteries. In *Meeting Abstracts*, number 15, pages 1154–1154. The Electrochemical Society, 2015.

[66] Rudolph A Marcus and Norman Sutin. Electron transfers in chemistry and biology. *Biochimica et Biophysica Acta (BBA)-Reviews on Bioenergetics*, 811(3):265–322, 1985.

[67] Rudolph A Marcus. On the theory of oxidation-reduction reactions involving electron transfer. i. *The Journal of Chemical Physics*, 24(5):966–978, 1956.

[68] Y Zheng and A Zaoui. How water and counterions diffuse into the hydrated montmorillonite. *Solid State Ionics*, 203(1):80–85, 2011.

[69] Christina Bergonzo, Kathleen B Hall, and Thomas E Cheatham III. Divalent ion dependent conformational changes in an rna stem-loop observed by molecular dynamics. *Journal of chemical theory and computation*, 12(7):3382–3389, 2016.

[70] Ralph P Seward and Ernest C Vieira. The dielectric constants of ethylene carbonate and of solutions of ethylene carbonate in water, methanol, benzene and propylene carbonate. *The Journal of Physical Chemistry*, 62(1):127–128, 1958.

[71] Man Liu, Peter J Chimtali, Xue-bin Huang, and Ru-bo Zhang. Structures and dynamic properties of the lipf6 electrolytic solution under electric fields–a theoretical study. *Physical Chemistry Chemical Physics*, 21(24):13186–13193, 2019.

[72] Michael J Weaver. Redox reactions at metal–solution interfaces. In *Comprehensive Chemical Kinetics*, volume 27, pages 1–60. Elsevier, 1988.

[73] John Edward Jones. On the determination of molecular fields ii. from the equation of state of a gas. *Proceedings of the Royal Society of London. Series A, Containing Papers of a Mathematical and Physical Character*, 106(738):463–477, 1924.

[74] James T Hynes. Outer-sphere electron-transfer reactions and frequency-dependent friction. *The Journal of Physical Chemistry*, 90(16):3701–3706, 1986.

[75] RD Armstrong. , jw diggle (ed.) oxides and oxide films, vol. 2, marcel dekker, new york (1973), 1974.

[76] Daniel F Calef and Peter G Wolynes. Classical solvent dynamics and electron transfer. 1. continuum theory. *The Journal of Physical Chemistry*, 87(18):3387–3400, 1983.

[77] Ron O Dror, Morten Ø Jensen, David W Borhani, and David E Shaw. Exploring atomic resolution physiology on a femtosecond to millisecond timescale using molecular dynamics simulations. *Journal of General Physiology*, 135(6):555–562, 2010.

[78] Philip J Pritchard, John W Mitchell, and John C Leylegian. *Fox and McDonald's Introduction to Fluid Mechanics, Binder Ready Version*. John Wiley & Sons, 2016.

[79] Jean Philibert. One and a half century of diffusion: Fick, einstein, before and beyond. *Diffusion Fundamentals*, 4(6):1–19, 2006.

[80] Charles Kittel et al. *Introduction to solid state physics*, volume 8. Wiley New York, 1976.

[81] Yuanyue Liu, Boris V Merinov, and William A Goddard. Origin of low sodium capacity in graphite and generally weak substrate binding of na and mg among alkali and alkaline earth metals. *Proceedings of the National Academy of Sciences*, 113(14):3735–3739, 2016.

[82] Markus Jackle and Axel Gross. Microscopic properties of lithium, sodium, and magnesium battery anode materials related to possible dendrite growth. *The Journal of chemical physics*, 141(17):174710, 2014.

[83] Daniel Stottmeister and Axel Groß. Strain dependence of metal anode surface properties. *ChemSusChem*, 2020.

[84] M. Arakawa, S. Tobishima, Y. Nemoto, M. Ichimura, and J. Yamaki. Lithium electrode cycleability and morphology dependence on current-density. *J. Power Sources*, 43(1-3):27–35, 1993.

[85] O. Crowther and A. C. West. Effect of electrolyte composition on lithium dendrite growth. *J. Electrochem. Soc.*, 155(11):A806–A811, 2008.

[86] Ingeborg Treu Røe, Sverre M Selbach, and Sondre Kvalvåg Schnell. Crystal structure influences migration along li and mg surfaces. *The Journal of Physical Chemistry Letters*, 2020.

[87] C. Brissot, M. Rosso, J. N. Chazalviel, and S. Lascaud. In situ concentration cartography in the neighborhood of dendrites growing in lithium/polymer-electrolyte/lithium cells. *J. Electrochem. Soc.*, 146(12):4393–4400, 1999.

[88] C. Brissot, M. Rosso, J. N. Chazalviel, and S. Lascaud. Concentration measurements in lithium/polymer-electrolyte/lithium cells during cycling. *J. Power Sources*, 94(2):212–218, 2001.

[89] RH Cork, DC Pritchard, and WY Tam. Local concentration measurements in electrochemical deposition using a schlieren method. *Phys. Rev. A*, 44:6940–6943, 1991.

[90] R. Feder. Equilibrium defect concentration in crystalline lithium. *Phys. Rev. B*, 2(4):828–&, 1970.

[91] Taylor A Barnes, Jakub W Kaminski, Oleg Borodin, and Thomas F Miller III. Ab initio characterization of the electrochemical stability and solvation properties of condensed-phase ethylene carbonate and dimethyl carbonate mixtures. *The Journal of Physical Chemistry C*, 119(8):3865–3880, 2015.